Laser-Based Far-Field Wireless Power Transfer for UAV Recharging: Architecture and Experimental Validation of the Pointing, Sensing, and Control System

*aerospace*

MDPI

*Article*

# Laser-Based Far-Field Wireless Power Transfer for UAV Recharging: Architecture and Experimental Validation of the Pointing, Sensing, and Control System

**Domenico Edoardo Sfasciamuro [1,*], Marco Lecce [2], Federico Zambelli [2] and Stefano Mauro [1]**

[1] Department of Mechanical and Aerospace Engineering, Politecnico di Torino, 10129 Torino, Italy; stefano.mauro@polito.it

[2] ORIS SRL, 10129 Torino, Italy; m.lecce@oris-space.com (M.L.); f.zambelli@oris-space.com (F.Z.)

* Correspondence: domenico.sfasciamuro@polito.it

**Abstract**

The rapid expansion of unmanned aerial vehicles (UAVs) applications in logistics, surveillance, and defense highlights the need for scalable and reliable energy delivery solutions. Conventional charging approaches constrain operational endurance and scalability, requiring frequent returns to base. This paper presents a laser-based wireless power transmission system designed to enable safe, contactless and efficient power transfer from ground to air. The main innovation of the work lies in the integration of an end-to-end architecture combining a high-power optical source, a hierarchical beam pointing framework with coarse and fine steering stages, and a receiver composed of sensing and energy conversion module mounted onboard the UAV. A further contribution is the adoption of a hybrid control strategy in which the reference position, obtained via RTK positioning, facilitates the coarse acquisition of the beam, whilst optical feedback from the receiver side enables precise alignment corrections. An experimental campaign is conducted to validate the main system functions under representative operating conditions. Beam propagation, pointing accuracy, and control response are characterized through laboratory and outdoor tests, including long-range spot measurements and closed-loop steering validation. The results demonstrate the technical feasibility of laser-based wireless energy transfer for UAV applications and provide an experimentally grounded framework for the development of persistent aerial operations in civil and defense scenarios.

**Keywords:** unmanned aerial vehicle; laser sensing systems; laser-based wireless power transmission; beam pointing; fine steering mirror; real-time kinematic positioning

Check for updates

Received: 1 June 2026
Revised: 17 July 2026
Accepted: 20 July 2026
Published: 24 July 2026



## 1. Introduction

Unmanned Aerial Vehicles (UAV) are increasingly deployed across logistics, inspection, surveillance, public safety and defense applications [1–3]. However, their operational endurance remains limited by battery energy density and by the need to return to fixed charging infrastructures. As UAV fleets diversify in size, payload, and mission profiles, conventional charging approaches, such as battery swapping, tethered solutions and ground-based docking, struggle to scale without introducing additional operational complexity, exposure and downtime. Far-field laser-based wireless power transfer (LWPT) has emerged as a contactless and dynamically reconfigurable alternative [4–6]: energy is transmitted along a line-of-sight optical link from a ground station to an onboard photovoltaic receiver that converts narrowband optical radiation into electrical energy. Compared to

 https://doi.org/10.3390/aerospace13080664

radio-frequency-based solutions, LWPT enables higher power densities and more compact transmission apertures, making it particularly suitable for applications requiring rapid deployment and precise energy delivery [7,8].

Academic studies have concurrently explored design spaces for optics-driven UAVs, including receiver materials, thermal constraints, and guidance/tracking strategies [7,8]. Despite recent demonstrations of laser-powered UAV flight and long-distance power beaming [9–12], several challenges remain. In particular, existing systems often lack scalability across different UAV classes, robust integration of pointing and control architectures, and experimental validation under realistic operational conditions [13]. Furthermore, the coupling between beam propagation, pointing accuracy, and system-level performance is not yet fully characterized in practical implementations.

In this context, this work presents a laser-based wireless power transfer system designed to enable in-flight energy delivery across multiple UAV categories. The proposed system integrates a high-power optical source, a hierarchical beam-pointing architecture combining coarse gimbal control and fine steering mechanisms, and a thermal management subsystem to ensure stable operation.

The main contributions of this paper are as follows:

- The design and integration of a complete LWPT architecture tailored for multi-platform UAV compatibility;
- A quantitative framework linking beam propagation, pointing performance, and energy delivery;
- An experimental validation campaign, including laboratory and outdoor tests, to characterize system performance in terms of feedback and pointing accuracy.

The remainder of the paper is structured as follows. Section 2 describes the system architecture and control framework. Section 3 presents the experimental campaigns and results. Section 4 discusses the findings and describes future developments.

## 2. Wireless Power Transfer Principles

This section summarizes the operating principles of the proposed laser-based wireless power transfer system and introduces the main physical quantities governing energy delivery from the transmitting source to the onboard receiver. The objective is to provide a system-level framework for interpreting the architecture and the experimental results discussed in the following sections.

### 2.1. Principle of Operation

Laser-based wireless power transfer relies on the transmission of optical energy through a line-of-sight free space link from a ground-based source to an onboard receiver. In the proposed architecture, electrical power is first converted into optical power by the transmitting source and emitted as a directed beam toward the UAV. The incident optical radiation is then intercepted by a photovoltaic receiver mounted on the UAV platform, where it is converted back into electrical energy that can charge the battery. Compared with conductive charging or docking-based approaches, this concept enables contactless energy delivery and can support opportunistic recharging without requiring the UAV to return to a fixed charging station. Unlike wired solutions, however, the effectiveness of the transfer depends not only on source power but also on beam propagation, geometric overlap between beam and receiver, and detection and tracking accuracy. As a result, wireless power transfer in this context must be treated as a coupled problem involving optics, sensing, pointing, and control. At system level, the transfer chain can be described as:

$$P_{el,in} \rightarrow \eta_{laser} \rightarrow P_{opt,tx} \rightarrow P_{opt,rx} \rightarrow \eta_{cells} \rightarrow P_{el,rx}, \quad (1)$$

https://doi.org/10.3390/aerospace13080664

where $P_{el,in}$ is the electrical input power at the transmitter, $P_{opt,tx}$ is the emitted optical power, $P_{opt,rx}$ is the optical power intercepted by the receiver, and $P_{el,rx}$ is the electrical power recovered after photovoltaic conversion and power conditioning. In our current system, the chain of efficiencies is as follows: $\eta_{laser} = 0.3$, $\eta_{cells} = 0.2$; at distances of just a few hundred meters, the effect of the environment on efficiency is negligible under standard conditions. Furthermore, in this paper, we neglect the electronic efficiency between the cell output and the battery input. This representation highlights that the transmitted optical power alone is not sufficient to characterize the system. The actual energy available at the UAV depends on how effectively the beam is generated, propagated, aligned, intercepted, and converted.

### 2.2. Transmitting Source and Beam Characteristics

The transmitting side of the system consists of a high-power optical source integrated with a beam-conditioning and steering chain. In practice, the transmitting source must satisfy two simultaneous requirements: it must deliver sufficient optical power density at the receiver plane, and it must maintain a beam geometry compatible with the pointing accuracy and receiver aperture available in realistic UAV operations. For this reason, the transmitting subsystem is not limited to the laser source itself, but includes the optical head and the conditioning elements required to shape the outgoing beam. These elements determine the beam radius, divergence, and footprint at distance, which directly influence the achievable irradiance at the receiver plane. For the infrared power-transfer beam, the theoretical propagation curves were generated using a Gaussian-beam approximation with beam-quality factor $M^2 = 1.1$ and wavelength $\lambda = 1070$ nm. The waist parameter $w_0$ should be interpreted here as the effective beam-waist radius after the beam-conditioning optics, rather than as the intrinsic waist of the bare laser source. The beam radius $w(z)$ at propagation distance $z$ can be expressed as

$$w(z) = w_0 \sqrt{1 + \left( \frac{M^2 \lambda\, z}{\pi w_0^2} \right)^2}, \tag{2}$$

where $w_0$ is the beam waist radius, $\lambda$ is the wavelength, and $M^2$ is the beam-quality factor. The corresponding beam diameter is

$$D(z) = 2w(z). \tag{3}$$

A first-order estimate of the average optical irradiance over the beam footprint can then be written as

$$I(z) \approx \frac{P_{opt,tx}}{\pi w^2(z)}, \tag{4}$$

showing that the beam radius has a direct impact on the power density available at the receiver. For a fixed transmitted optical power, a smaller beam footprint leads to higher irradiance and therefore potentially higher received power density. However, it also makes the transfer more sensitive to pointing errors and dynamic misalignment. Conversely, a larger beam footprint increases tolerance to tracking uncertainty, but reduces the optical power density available for conversion. This trade-off makes beamwidth one of the key design parameters of the transmitting source. In wireless laser power transfer, beam divergence cannot be optimized independently of the pointing strategy: a narrow beam improves energy concentration, while a wider beam improves robustness. The final design must therefore balance optical efficiency and alignment tolerance. In the present system, two optical beams are used with different roles. The infrared beam is the actual power-transfer channel and is therefore the relevant beam for link-budget evaluation and energy delivery. A visible beam is instead used as an auxiliary alignment and setup aid. As shown later in the experimental section, the visible beam exhibits a significantly larger divergence, consistent with its alignment role, whereas the infrared beam provides the beam characteristics relevant to power transfer.

### *2.3. Efficiency Considerations and System-Level Trade-Offs*

The efficiency of a laser-based wireless power transfer system is the result of multiple cascaded stages rather than a single conversion process. At system level, the end-to-end efficiency can be expressed as

$$\eta_{tot} = \eta_{eo}\,\eta_{prop}\,\eta_{int}\,\eta_{pv}\,\eta_{pc}, \tag{5}$$

where $\eta_{eo}$ is the electrical-to-optical conversion efficiency at the source, $\eta_{prop}$ accounts for free-space propagation losses, $\eta_{int}$ is the interception efficiency at the receiver plane, $\eta_{pv}$ is the optical-to-electrical conversion efficiency of the photovoltaic receiver, and $\eta_{pc}$ is the efficiency of the downstream power-conditioning stage. Among these factors, interception efficiency is particularly important in UAV applications because it is strongly affected by beam divergence, target motion, and residual pointing error. Even when the source and receiver operate efficiently, end-to-end performance may degrade significantly if the beam footprint is not properly aligned with the receiver aperture. For this reason, the efficiency of the present system is not treated as a property of the laser source alone, but as a system-level quantity coupled to optics, geometry, and control. A useful conceptual relation for the intercepted optical power is

$$P_{opt,rx} = \eta_{int}\,P_{opt,tx}, \tag{6}$$

where $\eta_{int}$ depends on the overlap between the beam footprint and the active receiver area. In practice, $\eta_{int}$ is influenced by beamwidth, distance, pointing accuracy, receiver geometry, and disturbances affecting both the transmitter and the UAV. From a design perspective, this introduces a fundamental system-level trade-off. Increasing the beam concentration can improve irradiance and potentially raise the useful received power, but at the cost of stricter pointing requirements. Increasing beam tolerance reduces the sensitivity to misalignment, but generally lowers the available power density at the receiver. Similarly, improving the photovoltaic conversion stage alone is insufficient if optical interception remains limited by tracking uncertainty. These coupled effects justify the hierarchical architecture adopted in this work, where source design, beam propagation, coarse pointing, fine steering, and receiver-side sensing are treated as interacting parts of the same wireless power transfer chain. For this reason, the present prototype is primarily intended to validate the enabling functions required for effective UAV laser recharging, namely, controlled beam propagation, receiver interception, hierarchical pointing, and closed-loop optical feedback. The experimental campaigns discussed later in the paper should therefore be interpreted not only as subsystem tests, but also as progressive validation steps toward an efficient end-to-end wireless power transfer architecture.

### *2.4. Receiver-Side Conversion*

On the receiving side, the incident laser beam is converted into electrical power by a dense photovoltaic receiver optimized for near-infrared operation. In the considered architecture, the receiving module is designed to provide relatively high voltage output within a compact area, which is advantageous for onboard integration and downstream power conditioning. Under representative illumination conditions, this class of receivers can achieve optical-to-electrical conversion efficiencies above 20%, with higher values possible under favorable beam uniformity, thermal management, and electrical load conditions.

https://doi.org/10.3390/aerospace13080664

As a result, the receiving module must be regarded not as a passive target, but as an active opto–electrical conversion stage whose performance depends on both the incoming beam characteristics and the local thermal environment.

### *2.5. Safety and Operational Constraints*

The use of high-power laser beams for wireless power transfer introduces safety requirements that must be considered together with efficiency performance. In particular, the transmitting source cannot be treated only as an energy-delivery device, since the resulting free-space optical link is also associated with eye-safety constraints, human exposure limitations, and operational restrictions in the surrounding airspace. At system level, the relevant safety factors include transmitted optical power, beam divergence, irradiance at accessible locations, exposure duration, line-of-sight geometry, and the possibility of unintended interception by operators, bystanders, or non-target aerial objects. For this reason, practical deployment of laser-based UAV recharging requires a controlled operating envelope in which beam generation, pointing, and enable logic are coordinated with access control and fail-safe interruption mechanisms. In the present work, safety is addressed as a system-level requirement rather than as a standalone component feature. The experimental campaigns therefore focus on validating the enabling functions of the architecture under controlled conditions, while the broader issues of certification, eye-safety classification, and operational authorization are recognized as essential aspects for future deployment-oriented developments.

## 3. System Architecture and Control Framework

This section presents the architecture and control strategy of the proposed laser-based wireless power transfer system. The focus is placed on the functional decomposition of the system, the sensing and tracking strategy, and the control architecture enabling precise beam pointing and stabilization during UAV recharging.

### *3.1. System Overview*

The system is composed of a ground-based laser transmitter and an onboard receiver integrated on the UAV. The ground segment is responsible for energy generation and beam pointing while the UAV hosts the energy conversion stage and sensors required for feedback and control. Energy is transferred through a line-of-sight optical link, which requires accurate alignment between the transmitter and receiver. This is achieved through a hierarchical control architecture that combines coarse pointing mechanisms and fine steering elements, supported by distributed sensors across both segments. Figure 1 illustrates the overall system architecture and highlights the functional decomposition between ground and airborne subsystems. The ground segment integrates positioning control and beam steering functionalities, while the UAV segment provides state estimation and feedback signals to the ground. Different types of interactions are represented, including mechanical couplings, electrical/control connections, and wireless communication links enabling real-time coordination between the two segments.

### *3.2. Ground Segment*

The ground segment is responsible for energy generation and beam pointing. It integrates three main functional subsystems: (i) a high-power optical source, (ii) a beam steering architecture, and (iii) a control and safety unit. The beam steering architecture follows a hierarchical approach. A coarse pointing stage provides large angular range and target acquisition capability, while a fine steering mechanism enables high-bandwidth corrections to compensate for residual misalignment and disturbances. This combination allows the system to achieve both wide coverage and high pointing accuracy. The optical chain includes beam shaping and conditioning elements to ensure controlled propagation and to match the receiver aperture at different distances. Safety mechanisms, such as interlocks and beam shutdown logic, are integrated at the system level to guarantee compliant operation: because the system operates with a high-power directed optical beam, safety is treated as a multi-layer function of the ground segment. In the proposed architecture, beam emission is enabled only under supervisory control and can be immediately interrupted through dedicated shutdown logic. These hardware interlocks are complemented by procedural and control-level safeguards intended to prevent unintended exposure and to maintain operation within a restricted and monitored test envelope. Therefore, the ground segment is responsible not only for beam generation and steering, but also for enforcing the conditions under which optical power transfer is permitted. A supervision and control unit coordinates all subsystems, handling mission logic, sensor fusion, and real-time command generation. The main hardware elements of the ground segment are shown in Figure 2.

Representative mechanical characteristics of the two pointing stages are summarized in Table 1.

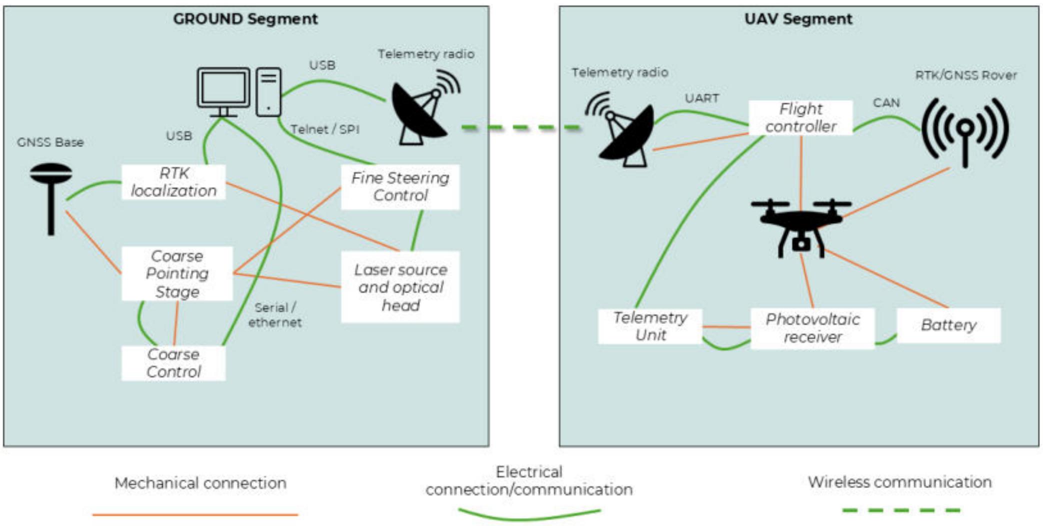


**Figure 1.** Functional architecture of the proposed laser-based wireless power transfer system, highlighting the main subsystems of the ground and UAV segments and their sensing, control, communication, and power-transfer interactions.


(**a**) Transmitter module. (**b**) Coarse pointing mechanism.

**Figure 2.** Ground segment hardware, including the optical transmitter and the coarse pointing subsystem.

**Table 1.** Representative mechanical specifications of the transmitter pointing chain.

| Subsystem | Parameter | Value |
|---|---|---|
| Coarse pointing stage | Range of motion | 360° (both axes) |
| | Pointing accuracy | 0.01° (0.1745 mrad) |
| | Repeatability | <0.005° (<0.087 mrad) |
| | Angular resolution | $1.5625 \times 10^{-4\circ}$ (2.73 µrad) |
| | Encoder count size | $5.556 \times 10^{-5\circ}$ (0.97 µrad) |
| | Maximum angular speed | 24°/s |
| Fine steering stage | Closed-loop tilt range | ±16 mrad (±0.916°) |
| | Closed-loop resolution | ≈0.3 µrad |

### 3.3. UAV Segment

The UAV segment hosts the energy reception and feedback subsystems required for closed-loop operation. The received optical power is converted into electrical energy through a photovoltaic receiver optimized for near-infrared laser illumination [14,15], followed by a power-conditioning stage for battery charging. The receiving module is based on a dense photovoltaic architecture designed to combine compact footprint, relatively high output voltage, and compatibility with laser power-transfer operation. From a functional standpoint, the energy receiving module performs the optical-to-electrical conversion stage of the wireless power transfer link. Its performance depends not only on the intrinsic conversion capability of the photovoltaic receiver, but also on the optical power density at the receiver plane, the uniformity of the incident beam, the operating temperature, and the electrical load conditions. Under representative operating conditions, this class of receiver can provide conversion efficiencies above 20%, making it suitable for compact UAV-oriented laser power reception. At the same time, thermal effects remain important, since elevated temperature can degrade conversion performance and must therefore be considered in system integration. In addition to energy conversion, the UAV provides real-time feedback to the ground segment. This includes vehicle pose information and optical measurements used for beam alignment. Onboard sensing enables estimation of the laser spot position on the receiver, supporting fine pointing corrections. The integration of sensing, communication, and energy conversion functionalities allows the UAV to actively participate in the control loop, improving robustness against disturbances and misalignment. The implemented UAV-side prototype is shown in Figure 3.

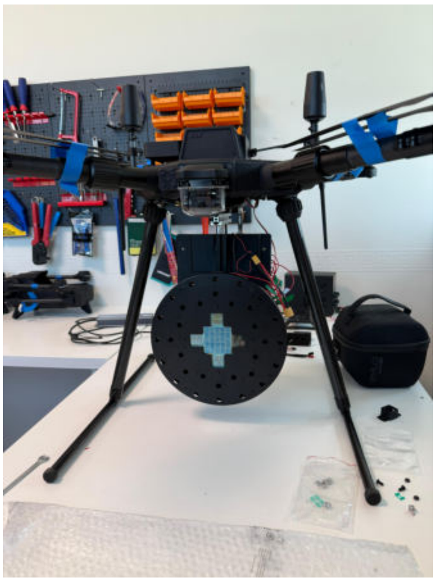

**Figure 3.** Prototype of the UAV receiver subsystem with integrated power reception interface.

https://doi.org/10.3390/aerospace13080664

### 3.4. Sensing and Tracking Strategy

Accurate beam pointing requires reliable estimation of the relative pose between the transmitter and the UAV. To this end, the system adopts a hybrid sensing strategy combining global positioning with local optical feedback. On the ground side, RTK positioning provides high-accuracy target localization in a global reference frame, with centimeter-level horizontal errors under favorable conditions, supporting coarse target acquisition and low-frequency tracking under nominal operating conditions [16,17]. RTK-GNSS techniques are widely used in UAV applications requiring accurate absolute positioning, although their performance can be affected by platform dynamics, signal visibility, multipath, and GNSS-degraded environments [16–18]. Therefore, the accuracy of RTK-based tracking alone may become insufficient in the presence of dynamic disturbances, long-range operation, or local alignment errors.

For this reason, onboard sensing is used to refine beam alignment at the receiver level. Several candidate approaches were considered for spot localization on the UAV, including photovoltaic cell matrices, photodiodes, quadrant detectors, and thermal sensors. Photovoltaic cell matrices can provide irradiance-aware feedback through distributed current measurements [8], whereas thermal sensors offer high robustness at the expense of limited temporal response. Photodiode-based and quadrant-detector sensing schemes provide representative detector-based approaches for optical tracking and laser spot localization, enabling high-bandwidth measurements with limited computational overhead [19–22]. Photodiodes therefore provide a suitable trade-off for the present implementation, despite requiring suitable optical protection against overload [7].

The adopted sensing strategy combines RTK-based target localization with receiver-side optical feedback, enabling hierarchical pointing control with improved robustness and accuracy. In this architecture, RTK measurements provide global target acquisition and coarse line-of-sight estimation, while local optical sensing compensates for residual alignment errors at the receiver plane. The interaction between the sensing, estimation, and control is summarized in Figure 4.

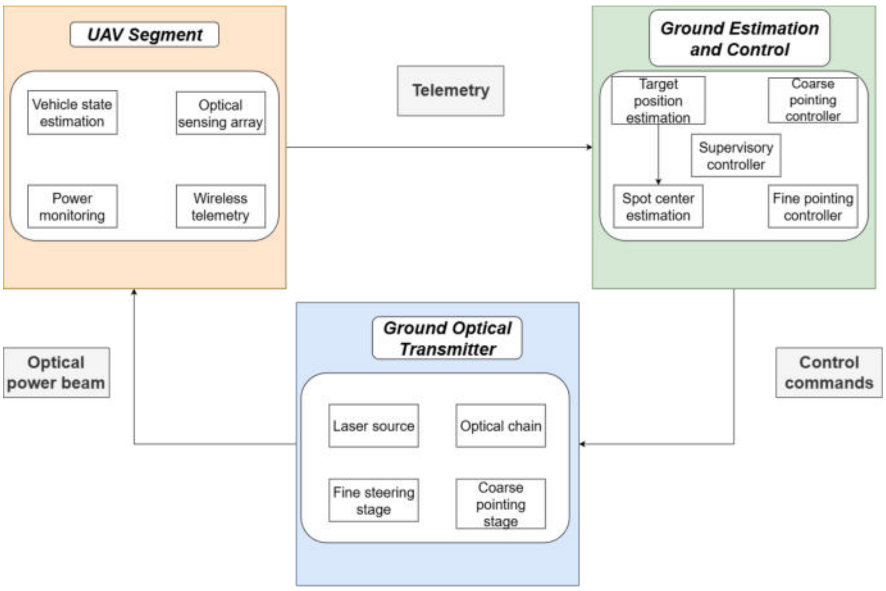


**Figure 4.** Functional block diagram of the sensing, estimation, and control architecture adopted for beam pointing and stabilization, combining RTK-based target localization on the ground side with receiver-side optical feedback for closed-loop beam alignment.

### *3.5. Coarse Pointing Formulation*

The Coarse Control System (CCS) is responsible for the geometric alignment of the laser beam with an arbitrary 3D target point, using a 2-DOF kinematic structure composed of yaw and pitch actuated joints. Coarse pointing for UAV optical links requires the integration of global target localization and frame calibration. In the present system, global target localization is provided by RTK and INS measurements, while the local pointing command is obtained through an inverse kinematics formulation of the ground-station mechanism. RTK-GNSS is commonly adopted in UAV applications requiring centimeter level positioning, although practical performance depends on platform dynamics, satellite visibility, multipath conditions, and the quality of correction data [16–18]. For this reason, accurate frame conversion between the global ENU frame and the local ground-station frame is treated as an explicit calibration step.

The laser is emitted along the local $\hat{y}$ axis of the terminal frame, and the pointing problem is formulated as an inverse kinematics task, solved through numerical optimization.

We model the device with homogeneous transforms $T_i \in SE(3)$ [23]. Let $q = [q_1, q_2]^\top$ be the yaw/pitch vector. The end transform to the laser source is

$$T_5(q) = T_0 \ \mathrm{Transl}(dx_0, dy_0, dz_0) \, R_z(q_1) \ \mathrm{Transl}(0, 0, dz_2) \, R_x(q_2) \ \mathrm{Transl}(dx_4, dy_4, dz_4),$$

with $T_0 = I_4$, where $\mathrm{Transl}(\cdot)$ is a pure translation, and $R_z(\cdot), R_x(\cdot)$ are elementary rotations. Write $T_5(q) = \begin{bmatrix} R_5(q) & p_5(q) \\ 0^\top & 1 \end{bmatrix}$, so the laser origin is $o(q) = p_5(q)$ and the laser direction is $d(q) = R_5(q)\,\hat{y}$, with $\hat{y} = (0, 1, 0)^\top$.

The kinematic chain used in the formulation is illustrated in Figure 5.

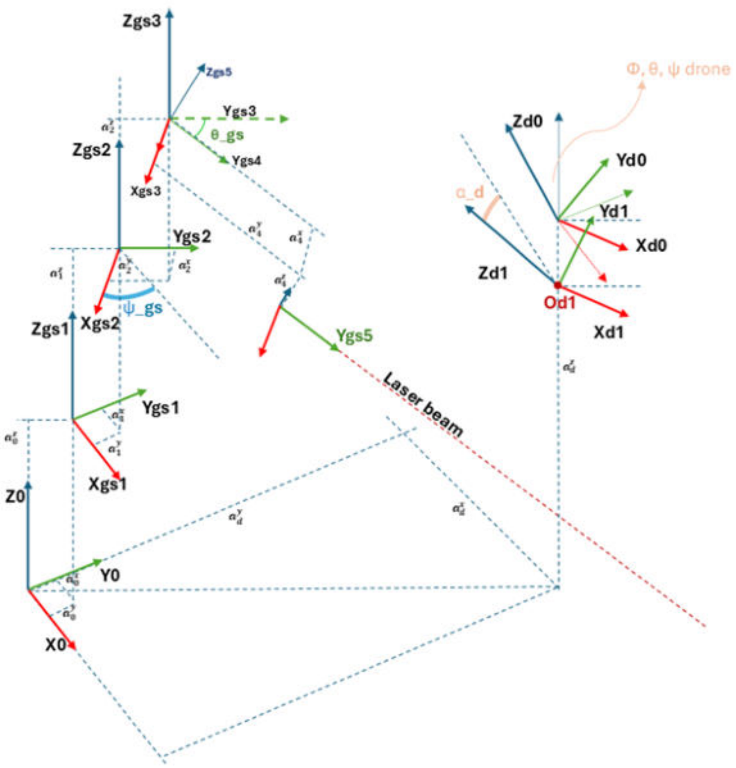


**Figure 5.** Kinematic model adopted for coarse beam pointing.

Given a target $p_{tar} \in R^3$ (in the following, $R$ denotes the set of real numbers), define the unit desired ray

$$v_{des}(q) = \frac{p_{tar} - o(q)}{\|p_{tar} - o(q)\|}.$$

A compact misalignment functional is

$$J(q) = 1 - v_{des}(q)^{\top} d(q),$$

which satisfies $J(q) = \frac{1}{2}\|v_{des}(q) - d(q)\|^2 = \sin^2\left(\frac{\theta(q)}{2}\right)$, where $\theta(q)$ is the angle between $v_{des}(q)$ and $d(q)$ [23]. The coarse pointing problem is the smooth, bound-free program

$$q^{\star} = \arg\min_{q \in R^2} J(q),$$

solved with a derivative-free or gradient-based method. Hardware conventions yield commanded angles $\Psi_{gs} = -q_1^{\star}$ (yaw) and $\Theta_{gs} = -q_2^{\star}$ (pitch).

The essential inverse kinematics procedure used to compute the coarse pointing commands is summarized in Algorithm 1. At each objective-function evaluation, the forward kinematics is computed for the current joint configuration, and the angular misalignment between the resulting laser direction and the target ray is evaluated. The process is repeated until the selected numerical solver satisfies its convergence criterion.

**Algorithm 1** Coarse-pointing inverse kinematics

**Require:** Target position $p_{tar}$, initial guess $q^{(0)}$, and kinematic parameters
**Ensure:** Ground-station commands $\Psi_{gs}$ and $\Theta_{gs}$
1: Define the objective function $\mathcal{J}(q)$
2: Compute $T_5(q)$ through the forward kinematic chain
3: Extract $o(q) = p_5(q)$ and $d(q) = R_5(q)\hat{y}$
4: Compute $v_{des}(q) \leftarrow (p_{tar} - o(q))/\|p_{tar} - o(q)\|$
5: Evaluate $J(q) \leftarrow 1 - v_{des}(q)^{\top} d(q)$
6: Compute $q^{\star} \leftarrow \arg\min_{q \in R^2} \mathcal{J}(q)$, initialized at $q^{(0)}$
7: $\Psi_{gs} \leftarrow -q_1^{\star}$
8: $\Theta_{gs} \leftarrow -q_2^{\star}$
9: **return** $\Psi_{gs}, \Theta_{gs}$

Let ${}^{E}r_{gt}$ be the Ground-Station-to-Target vector in the global ENU frame (from RTK/INS acquisition), and let ${}^{0}\mathbf{r}_{gt}$ be the same vector expressed in the local reference frame $RF_0$. We seek a rotation $R \in SO(3)$, where $SO(3)$ denotes the special orhogonal group in three dimensions, such that ${}^{0}r_{gt} = R\,{}^{E}r_{gt}$.

Frame alignment between heterogeneous coordinate systems is a standard problem in robotics, navigation, computer vision, and point-set registration. Full localization frameworks such as SLAM estimate platform pose by combining multiple sensing modalities, but they are not always required when the task is limited to estimating a rigid transformation between two calibrated frames [24,25]. In this work, the ENU-to-local conversion is formulated as an orthogonal Procrustes problem, for which the Kabsch algorithm provides a closed-form least-squares estimate of the optimal rotation between corresponding point sets [26–30].

Estimate $R$ from at least three non-collinear fiducials observed in both frames by solving

$$\min_{R \in SO(3)} \|RP - Q\|_F^2,$$

where $P, Q \in R^{3 \times n}$ ($n \geq 3$) collect centered point coordinates in ENU and local frames (i.e., each column set has zero centroid). Let $H = Q\,P^{\top}$ and $H = U\Sigma V^{\top}$ be its SVD. The optimal rotation is

$$R^{\star} = U\,D\,V^{\top}, \qquad D = diag\big(1,\,1,\,\det(UV^{\top})\big),$$

which enforces $R^{\star} \in SO(3)$ and rejects reflections. The ENU $\rightarrow$ local projection used by the CCS is then

$$^{0}r_{gt} = R^{\star}\,{}^{E}r_{gt},$$

ensuring consistency between global sensing and the local kinematic chain.

In the proposed architecture, the Kabsch-based estimate is used as a dedicated frame-calibration step within the coarse pointing chain, rather than as a full localization method. This targeted use is appropriate because RTK/INS already provides the global UAV position, while the dominant requirement for the CCS is the reduction of systematic misalignment between the global ENU frame and the local mechanical reference frame.

The cost $J$ is invariant to positive scaling of $p_{tar} - o(q)$ (purely angular), and the Kabsch estimate is unique when $H$ has full rank with non-degenerate singular spectrum. Numerical optimization can leverage analytic or automatic differentiation of $J$; however, the formulation above remains valid for black-box solvers, preserving compactness and robustness. In practical calibration, the use of non-collinear fiducials with sufficient geometric spread is important to avoid poorly conditioned estimates and to reduce the impact of measurement noise.

### *3.6. Fine Pointing and Feedback Control*

The Fine Control System (FCS) performs high-precision adjustments to maintain beam alignment during dynamic UAV maneuvers and external perturbations. Fine pointing in optical tracking systems typically relies on a closed-loop combination of local optical feedback and high-bandwidth actuation, where the accuracy and latency of the spot localization stage directly affect the achievable pointing performance [31–34]. The FCS closes the loop between sensor feedback and actuation by combining (i) a spot center estimation algorithm and (ii) a fine steering mirror (FSM) control law. The former extracts optical feedback from a concentric sensor array, while the latter maps this feedback into corrective angular commands for the FSM.

The present control law is intentionally simple: a proportional mapping between estimated spot displacement and mirror tilt; this is chosen for its low computational cost and ease of empirical tuning. The step-response data reported in Section 4.2.1 provide an initial time-domain indication of closed-loop behavior, showing convergence within a single commanded step and no observable overshoot across the tested range. A more complete control-theoretic characterization of the fine-pointing loop, including bandwidth, settling time, and disturbance-rejection performance, was not part of the present campaign and is left for future work.

The optical feedback is derived from a 32-element sensor array arranged in three concentric rings with radii $R_1, R_2, R_3$. The rings contain $n_1 = n_2 = 8$ and $n_3 = 16$ sensors, respectively, at positions $\{(x_i, y_i)\}_{i=1}^{32}$ obtained by polar-to-Cartesian conversion. Each sensor produces a calibrated and normalized signal $w_i \geq 0$, collected into vector $\mathbf{w} = (w_1, \ldots, w_{32})^{\top}$.

Laser spot center localization has been studied for decades in optical metrology, laser tracking, free-space optical systems, and detector guidance. Classical approaches that work on images fall broadly into two families: geometric methods, such as the Hough transform and circle fitting, and methods based on intensity, such as gray scale centroid and Gaussian fitting [35,36]. Geometric methods work well when the boundary of the spot is clearly defined, but noise, shape distortion, and partial truncation of the spot quickly degrade them. Centroid estimation is cheap to compute and remains a common choice when the system must run in real time, though it is sensitive to non-uniform illumination, background noise, saturation, and the specific thresholding scheme used [36,37]. Gaussian fitting can push localization accuracy further when the recorded beam profile is reasonably close to a Gaussian shape. It exploits the known intensity profile of the beam rather than treating the spot as a generic blob, and for this reason it is often preferred when the application calls for high precision in spot estimation [38].

In addition to camera-based pipelines, photodiode and quadrant-detector approaches provide a hardware-efficient alternative for real-time optical feedback. These methods estimate spot displacement directly from detector intensities and are well suited to embedded control loops, provided that nonlinear response, saturation, and signal imbalance are properly handled [19–22]. The adopted implementation follows this detector-based philosophy: instead of processing full-frame images, the algorithm operates directly on a sparse set of calibrated photodiode measurements distributed over the receiver plane.

An initial spot location $(u_x, u_y)$ is computed as the weighted centroid:

$$(u_x, u_y) = \frac{\sum_{i=1}^{32} w_i (x_i, y_i)}{\sum_{i=1}^{32} w_i}.$$

This centroid estimate provides a low-complexity first approximation and is consistent with classical intensity-weighted localization methods used in optical sensing and tracking systems [36,37].

To improve accuracy, the intensity profile is modeled as a bivariate Gaussian

$$G(x, y) = A \exp\left( -\frac{1}{2} \left[ \frac{(x-u_x)^2}{\sigma_x^2} + \frac{(y-u_y)^2}{\sigma_y^2} \right] \right),$$

linearized via logarithmic mapping into a quadratic form in $(x, y)$. Least-squares fitting yields coefficients from which $(A, u_x, u_y, \sigma_x, \sigma_y)$ are recovered [38]. Gaussian-based refinement is consistent with established spot localization methods and can improve the estimate when the sampled intensity distribution retains a sufficiently regular beam-like profile [19,21,38]. In the present implementation, the centroid estimate provides the initial localization, while the Gaussian refinement improves spatial resolution using the calibrated detector weights.

Robustness conditions. Two heuristics prevent false detections:

- COND1 (single-sensor dominance). If $\max_i w_i > \kappa_1 \cdot \max_{j \neq i} w_j$, the spot is assumed centered on the dominant sensor.
- COND2 (low variance). If $\mathrm{std}(w) < \kappa_2$, the signal is considered too faint, and $(u_x, u_y)$ is set to $(0, 0)$.

These checks are introduced to handle operating conditions in which centroid or Gaussian estimates may become unreliable, such as local saturation, weak illumination, or nearly uniform low-amplitude detector responses. Similar issues are commonly reported in spot localization algorithms based on thresholding, centroiding, and detector-intensity balancing [22,36,37].

The estimated spot coordinates $(x_s^p, y_s^p = u_x, u_y)$ are used to compute corrective angular commands for the FSM. A simplified proportional mapping is derived from the geometric relation between mirror tilt and spot displacement on the target plane [31–34,39]. Let $L = \|O_d\|$ be the nominal optical distance between mirror and target, with $O_d = (O_{d1,x}, O_{d1,y}, O_{d1,z})$. The angular corrections are computed as

$$\Delta\theta_y = \frac{x_s^p}{2L}, \qquad \Delta\theta_x = \frac{y_s^p}{2L\cos(\pi/4)}.$$

The commanded FSM state is then updated proportionally, until convergence:

$$\theta_y^{cmd} = \theta_y^{state} + K_y \, \Delta\theta_y, \qquad \theta_x^{cmd} = \theta_x^{state} + K_x \, \Delta\theta_x,$$

where $K_x, K_y > 0$ are proportional gains determined through empirical tuning. Saturation is enforced to guarantee $\theta_x^{cmd}, \theta_y^{cmd} \in [-16, 16]$ mrad, consistent with the physical stroke of the mirror actuators. Defaulting conditions set $\theta_x^{cmd} = \theta_y^{cmd} = 0$ in case of invalid inputs.

The fine pointing layer combines spot localization, geometric correction, and actuator constraints to reduce residual misalignment under dynamic operating conditions. The main practical advantage of the adopted estimator is that it combines the low computational cost of centroid-based localization with Gaussian refinement and validity checks, while operating directly on photodiode measurements rather than full-frame images. This makes it suitable for embedded closed-loop beam steering, without claiming general superiority over camera-based or multi-scale processing of images methods.

## 4. Experimental Validation

Given the power levels involved, all outdoor and long-range tests were conducted under controlled-access conditions and within predefined operational procedures intended to minimize unintended exposure to the optical beam. The test methodology relied on restricted beam paths, supervised activation logic, and immediate beam interruption capability. Furthermore, all personnel involved were wearing the correct safety equipment, including, but not limited to, protective goggles against laser radiation. The purpose of the present work is not to provide a full certification-oriented laser safety assessment, but to report the safety posture adopted during prototype-level validation campaigns. The experimental campaign was designed to validate the proposed system at multiple levels, including component robustness, beam propagation, pointing performance, sensing reliability and accuracy with telemetry integrity. Tests were conducted under both laboratory conditions and representative outdoor scenarios in order to assess the readiness of the overall laser-based recharging system. In particular, the outdoor campaigns were performed under daylight conditions.

### *4.1. Thermal Response of Optical Components*

Tests on components were performed to assess the thermal behavior and survivability of critical optics under IR illumination at representative power levels. The aim was to quantify their sensitivity to pre-existing defects and to confirm safety margins before integrating the optical components into the main optical system. The test conditions are summarized in Table 2. The mirror under testing was positioned outside the main optical bench in order to (i) avoid potential damage to the combiner in the unlikely event of an explosive failure and (ii) allow temperature measurements to be taken on the rear surface. Two levels of IR power were applied in separate cycles, with a cooling interval between cycles to return the mirror to ambient conditions. Two mirrors were tested: (i) the FSM mirror with a small crack on the edge and (ii) a new mirror with no visible defects. Temperature was monitored on front and rear sides; output optical power was recorded to detect any degradation during heating.

**Table 2.** Test conditions for the thermal assessment of representative steering mirrors under infrared illumination.

| Condition | Description |
|---|---|
| Laser power levels | 300 W and 1 kW (IR) |
| Cooling interval | Between runs, until the mirror returned to ambient temperature |
| Mirror positioning | External to the main optical bench |
| Rationale | Prevent collateral damage to the combiner and enable rear-side temperature measurements |
| Mirrors tested | FSM mirror (minor edge crack); new mirror (no visible defects) |
| Measurements | Front/rear temperature response; output optical power during exposure |

https://doi.org/10.3390/aerospace13080664

A markedly different thermal response was observed between the pristine mirror and the cracked unit. Under 1 kW exposure, the measured output thermal power showed a small dependence on mirror condition, with the new mirror yielding ∼860 W vs. ∼820 W for the cracked mirror (difference ≈ 5%). Temperature traces (front and rear) evidenced faster rise and higher steady value for the cracked mirror, consistent with additional local absorption near the defect. These results indicate that minor edge damage significantly affects thermal behavior under high irradiance. The observed ∼5% reduction in delivered optical power remains acceptable for prototype operation but must be accounted for in safety margins. The new mirror remained within acceptable temperature limits under continuous operation at 1 kW, supporting its use in subsequent tests.

### *4.2. Beam Propagation and Fine Pointing Validation*

#### 4.2.1. Beam Diameter Characterization

Beam propagation was experimentally characterized by measuring the spot diameter as a function of range for both infrared and visible alignment beams. The IR and green laser sources were characterized during the field trials with a camera-based estimator that returns spot diameter and center at multiple ranges. A checkerboard placed on the spot plane provided metric referencing, and accuracy was verified against ellipses of known size and position; the mean error on diameter and center was below 2% in calibration. For the IR beam the internal slide of the combiner optics was set to 11 mm, close to the minimum-radius condition used during the campaign.

As analytical reference, the $1/e^2$ radius is modelled as

$$w(z) = w_0 \sqrt{1 + \left( \frac{M^2 \lambda\, z}{\pi w_0^2} \right)^2}. \tag{7}$$

and the diameter is $D(z) = 2\, w(z)$. Because the image thresholding yields a contour near the 86% power level, the measured diameter remains approximately proportional to $2\, w$ for a Gaussian spot.

Table 3 summarizes the measured diameters and the linear fits adopted for quick prediction within the tested range:

$$\begin{aligned} D_{IR}[mm] &\approx 1.236\, z[m] + 9.93, \quad R^2 = 0.996, \\ D_G[mm] &\approx 4.493\, z[m] + 45.98, \quad R^2 = 0.913. \end{aligned} \tag{8}$$

The significantly larger divergence observed for the green beam is consistent with its role as an alignment source, characterized by lower beam quality and larger effective divergence compared to the infrared power beam. Beyond ∼40 m, the measurements closely follow the theoretical propagation model, supporting their use for link-budget estimation. Deviations at short range are attributed to thresholding effects, alignment tolerances, and near-field propagation behavior. In Figure 6, in addition to the nominal Gaussian-beam propagation curves, we also report corrected trends that account for an effective atmospheric broadening term. These additional curves are not intended as a full turbulence model, but rather as a first-order indication of how free-space propagation disturbances may increase the beam footprint at distance. Within the tested range, the corrected curves remain close to the nominal propagation trend for the infrared beam, while the visible beam shows a more pronounced sensitivity to effective broadening.

https://doi.org/10.3390/aerospace13080664

**Table 3.** Test campaign: Measured spot diameter versus distance and linear-fit interpolation at 100 m and 150 m. Some data relating to the green laser are not available due to the excessive divergence of this laser beyond 30 metres.

| Distance $z$ [m] | $D_{IR}$ [mm] | $D_G$ [mm] |
|---|---|---|
| 9.4 | 20.6 | 80.2 |
| 14.4 | 29.4 | 122.7 |
| 24.4 | 38.9 | 151.6 |
| 44.4 | 62.7 | n/a |
| 59.4 | 86.9 | n/a |
| 74.4 | 104.0 | n/a |
| 85.0 | 112.0 | n/a |
| 100.0 | 133.6 (interp.) | 495.3 (interp.) |
| 150.0 | 195.4 (interp.) | 514.6 (interp.) |

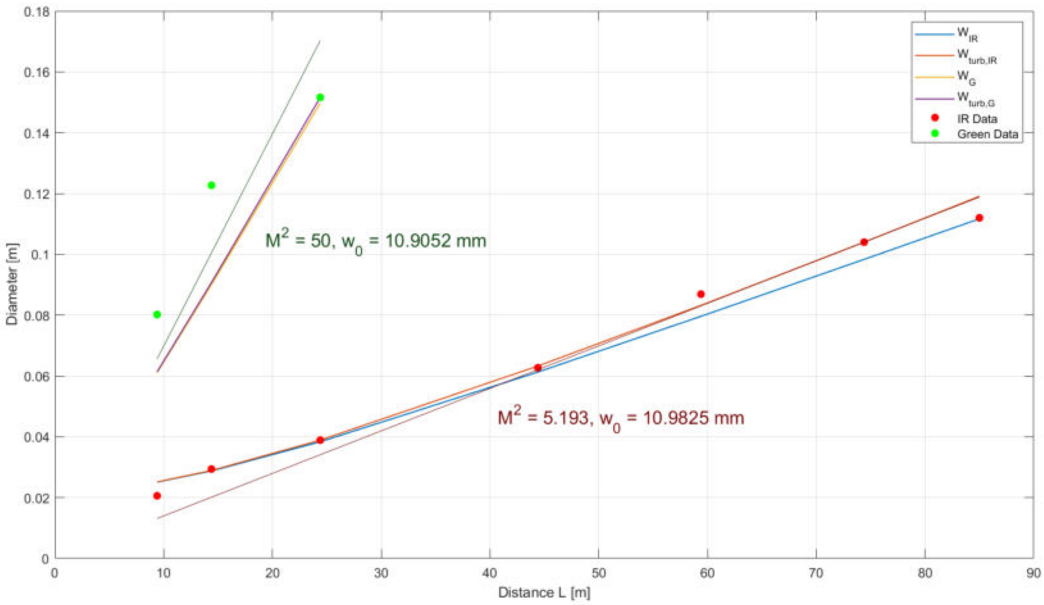


**Figure 6.** Test campaign: Spot diameter vs. distance for IR and green beams with linear fits and reference theoretical curves. Green and red lines represent the interpolation of IR and green data.

#### 4.2.2. FSM Command–Spot Displacement Correlation

The correlation between Fast Steering Mirror (FSM) commands and the resulting spot displacement at range was experimentally quantified during the trials using the IR beam (combiner slide at 11 mm). A calibrated camera-based estimator retrieved the spot center $(X, Y)$ on the target plane while commanding steps along the FSM $Y$ axis. The checkerboard metric reference yielded a mean error below 2% on center estimation in calibration.

For the single mirror two-axis scanner adopted here, the mapping between FSM rotations $(\alpha_x, \alpha_y)$ and spot coordinates $(X, Y)$ on a plane orthogonal to the nominal beam at distance $L$ is as follows [39]:

$$\begin{aligned} X &= L\,\frac{\cos^2\alpha_y\,\sin(2\alpha_x) - \sin^2\alpha_y\,\sin(2\beta)}{\cos^2\alpha_y\,\cos(2\alpha_x) - \sin^2\alpha_y\,\cos(2\beta)}, \\ Y &= L\,\frac{\cos(\beta-\alpha_x)\,\sin(2\alpha_y)}{\cos^2\alpha_y\,\cos(2\alpha_x) - \sin^2\alpha_y\,\cos(2\beta)}, \end{aligned} \tag{9}$$

where $\beta$ is the incidence angle (about 45° in our setup). Figure 7 shows the geometric configuration used for the single-mirror two-axis scanner model.

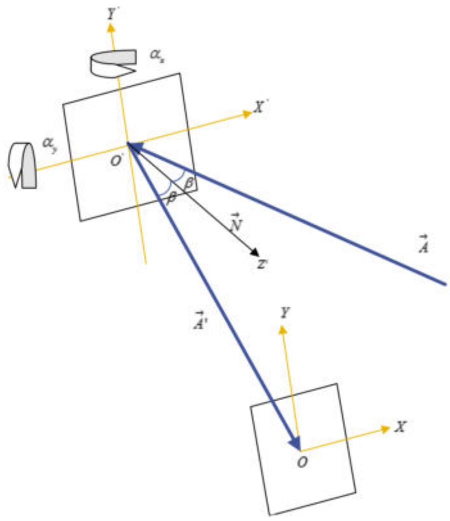


**Figure 7.** Geometry of the single-mirror two-axis scanner showing angles $(\alpha_x, \alpha_y)$ and incidence $\beta$ [39].

For small scan angles ($|\alpha_x|, |\alpha_y| \ll 1$) and $\beta \simeq 45^\circ$, Equation (9) linearizes to

$$X \approx 2L\,\alpha_x, \qquad Y \approx 2L\,\alpha_y\,\cos\beta, \tag{10}$$

highlighting the different sensitivity along $Y$ due to the $\cos\beta$ factor. At $L = 80$ m, this gives practical gains $k_x = 2L \simeq 160$ m/rad and $k_y = 2L\cos\beta \simeq 113$ m/rad (i.e., 160 mm/mrad and 113 mm/mrad).

A Y-only sequence from 0 to 400 mm in nominal 50 mm steps was executed at $L \simeq 80$ m while logging the measured spot centre and diameter. The increments track the nominal steps with residuals within 2–9%, and the cross–axis drift in $X$ over the full sweep remains ∼6 mm, indicating limited coupling. The data of the measured $X$ and $Y$ are in Table 4.

**Table 4.** IR spot center at ∼80 m under Y steps. Incremental error is computed vs. the 50 mm nominal step.

| Command Y [mm] | Command Y [mrad] | Spot Diameter [mm] | Measured X [mm] | Measured Y [mm] | Step Error [%] |
|---|---|---|---|---|---|
| 0 | 0.000 | 110 | −180 | 431 | - |
| 50 | −0.442 | 111 | −181 | 386 | 9 |
| 100 | −0.884 | 110 | −182 | 337 | 5 |
| 150 | −1.326 | 114 | −180 | 289 | 5 |
| 200 | −1.768 | 113 | −180 | 244 | 6 |
| 250 | −2.210 | 111 | −183 | 193 | 5 |
| 300 | −2.652 | 114 | −184 | 139 | 2 |
| 350 | −3.094 | 110 | −185 | 94 | 4 |
| 400 | −3.536 | 116 | −186 | 44 | 3 |

These results confirm the validity of the small-angle approximation and demonstrate that the FSM provides predictable and weakly coupled beam steering, enabling reliable fine-pointing control at long distances.

### *4.3. Coarse Pointing Validation*

This set of experiments was designed to validate the coarse pointing strategy introduced in Section 3.5. The objective was to assess the ability of the ground station to align the laser beam toward a UAV target based on RTK-derived positioning.

#### 4.3.1. Outdoor Dynamic Test in Flight Cage

The first campaign was conducted in the open-air Voliera flight cage. A precomputed rotation matrix was used to transform the Ground-Station-to-Target vector from global ENU coordinates into the local reference frame of the 2-DOF kinematic chain (to be used in the previously introduced inverse kinematics algorithm). This rotation matrix was derived from RTK measurements of three non-collinear fiducials fixed to the ground station frame, together with the global position of the UAV.

During testing, the UAV was commanded to follow trajectories at an average distance of 15 m. Angular and positional errors of the robotic pointing were recorded. Two main categories of errors were identified:

- Dynamic positioning errors, occurring during lateral UAV motion. These were largely due to the velocity saturation imposed in the yaw/pitch control loop for safety.
- Static positioning errors, observed during UAV hovering. These were attributed to a combination of optical path misalignments (micrometric screw calibration), inverse kinematics approximations, and possible inaccuracies in the ENU $\rightarrow$ local transformation.

Overall, the observed error magnitude ranged between 10 cm and 80 cm, significantly exceeding the expected RTK accuracy and indicating the presence of systematic error sources within the pointing chain. This discrepancy motivated a structured decomposition of the error budget, aimed at isolating the dominant contribution within the sensing, calibration, and actuation chain. The optical alignment procedure used during the outdoor campaign is illustrated in Figure 8. The figure shows the two-axis motion control system, with the optical chain mounted on top. In the first image, you can see the green laser inside the optical chain, and in the last image, the same laser correctly aligning with the receiver mounted beneath the drone.

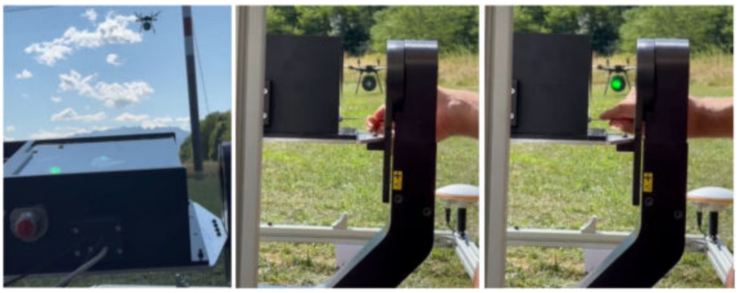

**Figure 8.** Optical alignment procedure illustrating mechanical adjustment of the beam with respect to the reference frame. (**Left**): Optical chain mounted on the pitch stage of the 2-axis gimbal while pointing toward the UAV using the green aiming laser. (**Center**) and (**Right**): Calibration of the Fine Steering Mirror through two micrometric adjustment screws, used to center the beam on the receiver panel after coarse pointing based on the RTK target position and the inverse kinematics solution.

More specifically, the figure comprises three photographs of the same experimental system. The optical chain is mounted on the second, pitch-actuated stage of the two-axis gimbal, so that the coarse yaw–pitch mechanism provides the primary line-of-sight orientation, while the optical components mounted on the pitch stage perform the subsequent beam-alignment functions. In the left-hand image, the gimbal is pointing toward the UAV in flight and the green aiming laser is switched on, providing a visible indication of the direction produced by the coarse pointing system.

The central and right-hand images illustrate the calibration of the Fine Steering Mirror (FSM). Its orientation relative to the optical chain is adjusted by rotating two micrometric screws, which independently modify the angular attitude of the mirror. This adjustment is performed while the two-axis gimbal is oriented according to the pointing direction computed by the inverse kinematics algorithm for the current desired target position $\mathbf{p}_{des}$, obtained from the RTK position transmitted by the UAV. The micrometric screws are then used to compensate for residual optical misalignment and to steer the visible aiming beam toward the center of the receiver panel mounted beneath the UAV. Thus, the illustrated procedure aligns the fine optical pointing direction with the coarse line of sight generated from the RTK-based target position and the inverse kinematics solution.

Following the outdoor results, a structured indoor campaign was initiated to test each suspected error contribution in isolation. Three main potential sources were identified:

1. Absolute error in the RTK positioning system. Both systematic and correction errors were considered.
2. Errors in inverse kinematics and two-axis actuation. Possible inaccuracies in control or CAD-derived mechanical parameters.
3. Errors in the ENU → local rotation matrix. Inaccuracies in the frame transformation used by the coarse control system.

#### 4.3.2. RTK Validation with Reference Point on UAV

To verify whether the RTK positioning system could be the source of the observed errors, a dedicated validation campaign was carried out. The UAV reference point was chosen as the rear tip of the left landing gear, located at an offset from the GNSS antenna phase center ($x = -23$ cm, $y = 40$ cm, $z = -59.5$ cm). This ensured that the RTK-derived position could be consistently related to a physical marker on the vehicle. Two structured tests were performed:

1. Test along the North axis (constant East coordinate). A set of positions was defined along the geographic North direction, keeping the East coordinate fixed. Distances were measured with a tape measure, and the UAV was placed at each predefined point with the reference marker aligned. At every position, coordinates were recorded via a centimeter-level RTK system. The following comparisons were made:
   - Drone-computed $x, y$ coordinates (after reference point transformation) vs. ground-truth tape-measured positions;
   - RTK-derived $z$ coordinate vs. ground-truth altitude.
2. Test along the East axis (constant North coordinate). Similarly, positions were defined along the geographic East direction with constant North coordinate. Distances were measured with tape, the UAV reference point was aligned, and RTK-derived coordinates were acquired at each position. Again, both horizontal coordinates and altitude were compared against ground-truth.

The results in Table 5 showed that both horizontal and vertical discrepancies between RTK measurements and ground-truth were within a few centimeters, consistent with the expected accuracy of the RTK receiver. Based on these results, both the ENU position estimates and the rotation matrix used to translate the UAV position onto the target were deemed reliable. RTK positioning was therefore excluded as the dominant source of the observed pointing errors.

**Table 5.** Summary of RTK validation against ground-truth reference positions. H: Horizontal; V: vertical.

| Direction | Range [m] | N | Mean H Err [m] | Max H Err [m] | Mean V Err [m] |
|---|---|---|---|---|---|
| North ($\Delta E = 0$) | 5–15 | 3 | 0.027 | 0.046 | 0.111 |
| East ($\Delta N = 0$) | 5–20 | 3 | 0.018 | 0.040 | 0.192 |

#### 4.3.3. Target-Grid Benchmark

To validate the inverse kinematics algorithm on real hardware, a structured grid of target points was defined on a 7 × 3 panel arrangement aligned with the local reference frame of the ground station. The corresponding target coordinates and commanded angles were used to validate the inverse kinematics model. To obtain a repeatable physical benchmark for the inverse-kinematics validation, the target grid was implemented using three planar panels mounted on a horizontal support beam. The beam was positioned so as to remain perpendicular to the ($Y_0$) axis of the local ground-station reference frame introduced in Figure 5. The three panels were then fixed on the beam with their surfaces also kept perpendicular to ($Y_0$), thus defining a common target plane orthogonal to the nominal pointing direction. Starting from this predefined geometry, the panels were translated by known distances along the horizontal beam. This made it possible to mark benchmark target points directly on the panel surfaces while preserving, for each marked point on a given panel, a constant distance from the origin of the local reference frame. The resulting arrangement provided a structured set of target points with known relative positions, suitable for comparing the angles computed by the inverse-kinematics model with the actual beam impact locations observed during the test. The adopted setup therefore allowed the inverse-kinematics chain to be validated independently from UAV motion and RTK uncertainty, by using a fixed, measurable, and repeatable target grid aligned with the local mechanical reference frame of the ground station.

The experimental test bench used for target-grid validation is shown in Figure 9.

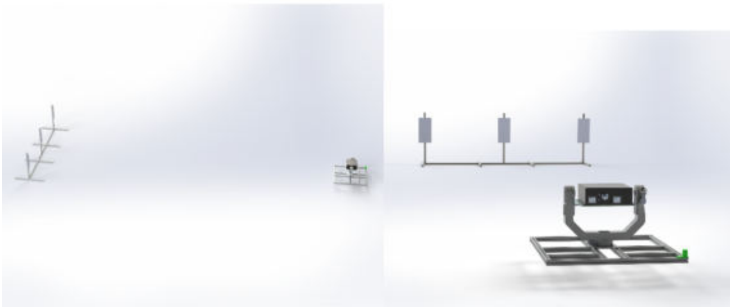

**Figure 9.** Experimental test bench used for coarse pointing validation on predefined target points.

#### 4.3.4. Inverse Kinematics Validation

The computed angles were first compared against simulation outputs assuming perfectly aligned panels: discrepancies were negligible (hundredths of a degree). The same procedure was repeated on the physical testbench by directing the beam to the defined grid points, and low-exposure images of the laser spots were acquired. Real-world errors were consistently around 1 cm, in line with RTK positioning noise, confirming that neither inverse kinematics nor actuation inaccuracies were the dominant source of error. These results confirm that the inverse kinematics formulation is not a limiting factor in the overall pointing accuracy. In Figure 10, there are representative low-exposure spot images.

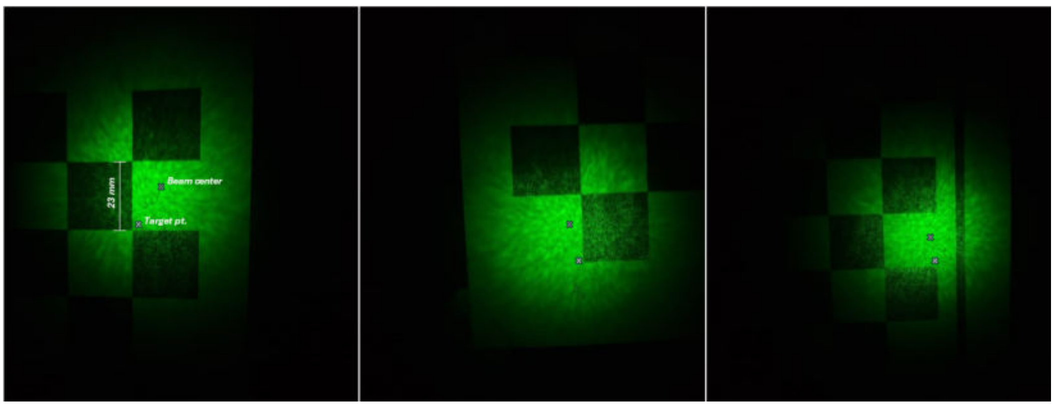


**Figure 10.** Representative low-exposure spot images used for manual assessment of inverse kinematics pointing error.

#### 4.3.5. Laser Meter Calibration

The laser meter system provided ground-truth 3D coordinates of selected target points. These measurements were then compared to "manual" reference values obtained by carefully positioning the panels with respect to the local ground-reference frame in the laboratory. Table 6 reports the results: the average RMS difference was 2.8 cm, validating the laser-based setup as a practical and reliable benchmark tool for field calibration.

**Table 6.** Comparison between laser-based and manual reference measurements.

| Point | $\Delta x$ [m] | $\Delta y$ [m] | $\Delta z$ [m] |
|---|---|---|---|
| F0 | 0.011 | −0.005 | −0.011 |
| B1 | 0.009 | −0.010 | −0.016 |
| D3 | −0.132 | 0.018 | −0.202 |
| A3 | 0.148 | 0.021 | 0.171 |
| Avg. RMS | | 0.028 | |

These comparisons confirmed that the target coordinates reconstructed via the laser meter were consistent with manual alignment within a few centimeters. Consequently, the laser meter was adopted as the standard calibration instrument for subsequent Kabsch-based refinements of the ENU $\rightarrow$ local rotation matrix.

#### 4.3.6. Indoor Kabsch Algorithm Validation

Since RTK accuracy and inverse kinematics had been independently validated, emphasis was finally placed on the ENU $\rightarrow$ local rotation matrix as the ultimate potential source of error. To refine this transformation, the orthogonal Procrustes (Kabsch) algorithm was implemented and validated under both simulated and real conditions.

#### 4.3.7. Simulation Tests

Before applying the Kabsch-based calibration to experimental data, the algorithm was first validated in simulation under controlled conditions. A set of synthetic three-dimensional fiducial points was generated in a reference local frame, and known rotational perturbations were applied to obtain a second set of corresponding points expressed in a misaligned frame. The two point sets were then used as input to the orthogonal Procrustes formulation described in Section 3.5. Since the imposed transformation was known a priori, the reconstructed rotation matrix could be directly compared with the ground-truth rotation. This allowed the numerical implementation to be tested independently from RTK uncertainty, laser meter accuracy, mechanical alignment errors, and measurement noise. The recovered rotation matrix matched the imposed transformation with element-wise errors below ($10^{-8}$), confirming the correctness and numerical stability of the implementation in ideal conditions. The simulation therefore served as a preliminary verification step, ensuring that any residual error observed in the following experimental calibration would mainly originate from measurement and setup uncertainties rather than from the Kabsch algorithm itself.

#### 4.3.8. Outdoor Kabsch Tests in Real Conditions

This section introduces the outdoor validation of the global to local frame alignment using the Kabsch method under real operating conditions. The test was designed to verify whether the calibration procedure introduced in Section 3.5 could reduce systematic misalignment between the RTK-derived ENU target coordinates and the ground station local mechanical reference frame.

We collected ten non-collinear reference points by positioning the UAV at diverse bearings, ranges, and altitudes around the ground station, in order to span a broad geometric baseline. For each point, a laser range finder provided the line of sight distance to the target while the onboard RTK delivered centimeter-level georeferenced positions. This configuration is consistent with the use of RTK-GNSS as a high accuracy global positioning layer for UAV applications, while acknowledging that frame calibration remains necessary when global coordinates must be projected into a local pointing mechanism [16–18].

The paired observations in the global ENU frame and in the local ground station frame were then used to estimate the rigid rotation and translation with the Kabsch algorithm. The protocol was designed to maximize angular diversity and to avoid degeneracies, making the calibration more resilient to sensor noise and small setup drifts. This is consistent with rigid point-set registration practice, where the quality and spatial distribution of correspondences strongly affect the conditioning of the estimated transformation [25]. The resulting transform is subsequently used by the coarse pointing chain and serves as the basis for the fine steering experiments reported later. The outdoor calibration configuration used during tests is illustrated in Figure 11.

**Figure 11.** Outdoor validation setup during UAV-assisted calibration of the reference frame transformation.

4.3.9. Calibration Outcome

The calibration results indicate that inaccuracies in the ENU-to-local frame transformation were the dominant source of the pointing errors observed in the initial outdoor tests. After applying the Kabsch-based calibration, the residual static targeting error was reduced to the same order of magnitude as the expected RTK positioning uncertainty, namely, a few centimeters under the tested conditions. This confirms that the inverse kinematics formulation and the RTK positioning layer were not the limiting factors once the global to local frame alignment was properly calibrated.

### *4.4. Receiver-Side Sensing and Telemetry Validation*

Experiments on the receiver side assessed the wireless telemetry link and the accuracy of the localization of the spot thanks to the photodiode array. It is important to distinguish between the two main functions of the receiver subsystem: the photovoltaic receiving module, which governs optical to electrical energy conversion, and the photodiode sensing layer, which supports spot localization and fine alignment feedback. Although physically integrated within the same onboard subsystem, these two functions address different aspects of system performance, namely, energy reception and beam tracking.

#### 4.4.1. Telemetry Link Performance

The receiver-side prototype was equipped with a microcontroller-based telemetry unit tasked with streaming data from the photodiode channels and current-monitoring sensors through a low-latency wireless link. The communication was implemented using ESP-NOW, a connectionless Wi-Fi-based protocol. During field operation, each telemetry frame had a total payload of 239 bytes and included 59 single-precision floating-point values representing the photodiode signals and the current and voltage measurements of the photovoltaic cells, together with a three-byte timestamp encoding hours, minutes, and seconds. The payload therefore consisted of 236 bytes of floating-point data and 3 bytes of timing information, remaining within the 250-byte packet-size limit adopted in the implemented configuration. The measured inter-packet interval during field operation ranged from approximately 70 to 150 ms, corresponding to an effective update frequency of approximately 6.7–14.3 Hz and a useful payload rate of approximately 12.7–27.3 kb/s.

A series of link-quality tests were carried out at different distances between transmitter and receiver, each lasting 90 s. For these dedicated BER tests, the transmitted payload was reduced to a representative diagnostic packet of approximately 125 bytes. This reduced packet was sent at a nominal rate of approximately 50 Hz, corresponding to an application payload rate of approximately 50 kb/s. The reduced packet configuration was used only to evaluate communication reliability as a function of distance and was therefore different from the complete 239-byte telemetry frame used during field operation. For each distance, the received packet count, number of errors, and Bit Error Rate (BER) were logged.

The results showed robust communication performance across all tested distances up to 170 m, in particular:

- At 1 m, approximately 4500 packets were transmitted with zero errors (BER = 0).
- At 30 m, over 4400 packets were received in 90 s with no observable packet loss.
- At 90–110 m, performance remained stable with packet counts above 4200 and BER = 0.
- Even at 170 m, the system maintained communication, with 3946 packets successfully received and no errors.

These results confirm that the low-latency wireless telemetry link was not a limiting factor in the acquisition chain, ensuring reliable throughput compatible with the intended real-time telemetry needs.

#### 4.4.2. Photodiode Array Response

To quantify the spatial resolution of the photodiode array, a dedicated benchmark test compared the array's estimates of the centroid and the Gaussian spot with an independent reference based on camera. The reference used a calibrated 255 mm target disk and a green 520 nm laser, intentionally decollimated to a footprint ($\sigma$ = 25 mm) comparable to the photodiode spacing, at a laboratory distance of 6.5 m; the FSM placed the spot at various positions, covering the central, intermediate and peripheral areas of the target. Two photodiodes were missed caused by signal distortion, as shown in Figure 12 , along with the general photodiode layout. Two data acquisition campaigns were carried out under different ambient lighting conditions: stable evening illumination (number of smples $N = 46$) and variable daylight ($N = 26$). Table 7 summarizes the resulting Euclidean localization error, defined as the planar distance between the spot center of the reference point derived from the camera and the estimate provided by the photodiode array.

**Table 7.** Photodiode-array spot-localization error against the camera reference.

| Condition | N | Mean Error [mm] | Median [mm] | RMSE [mm] | P95 [mm] |
|---|---|---|---|---|---|
| Stable (evening) light | 46 | 18.1 | 17.6 | 20.2 | 31.0 |
| Variable daylight | 26 | 18.6 | 18.4 | 20.6 | 32.9 |

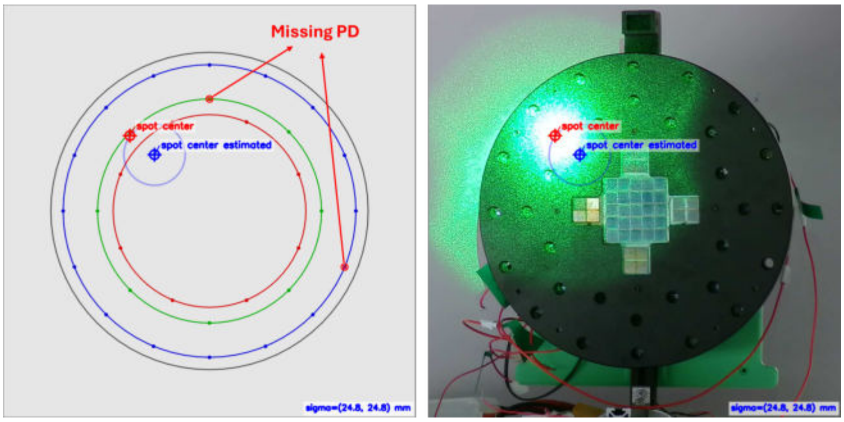


**Figure 12.** Representative single-sample panel: Raw camera image with photodiode-array-estimated spot center overlaid (**Right**). Photodiode layout with concentric rings R1 (red), R2 (green) and R3 (blue) and Missing PhotoDiodes highlighted (**Left**).

Accuracy remained essentially unchanged under different lighting conditions, confirming that the normalization of the baseline and sensitivity for each channel adequately compensates for drift caused by ambient light, including the more pronounced contribution from the background and reflections visible in daylight, as shown in Figures 13 and 14. The errors showed a radial trend only in daylight conditions, increasing from 10 mm near the target center to ∼25–30 mm near the outer photodiode ring (≥90 mm radius), as shown in Figure 15 and 16, consistent with the reduced number of illuminated channels, and hence reduced information content, as the spot approaches the array boundary. Errors, as shown in Figures 17 and 18, show no comparable systematic trend with angular position, aside from isolated outliers attributable to local gain mismatch or partial channel occlusion. The error distributions in both conditions were unimodal, with a median around 18 mm and a 95th percentile error below 33 mm (Figures 19 and 20). A representative single-sample panel, as also shown in Figure 12, illustrates the estimator output overlaid on the raw camera image, showing the recovered spot center relative to the visible illumination pattern. These results provide quantitative localization accuracy (mean error ≈ 18 mm, $RMSE \approx 20$ mm over a 255 mm target) and confirm that the photodiode array supports beam detection with spatial resolution—with a known and limited accuracy—suitable as input for the fine-pointing feedback loop, whilst identifying the positioning at the edges of the aperture as the main factor limiting accuracy and on which to focus future improvements. It should be noted that the benchmark was carried out at a laboratory distance of 6.5 m using a deliberately decollimated beam, chosen to produce a spot on the receiver plane comparable to the distance between the photodiodes; extending this characterization to operational distances is identified as a topic for future work.

### *4.5. Outdoor Disturbance and Long-Range Considerations*

The present experimental campaign was scoped to validate the enabling functions of the architecture at the tested range (up to 170 m for telemetry, up to 150 m for beam-propagation characterization), and two aspects relevant to future operational deployment were not systematically characterized. First, ambient wind conditions during the outdoor flight-cage tests were not instrumented; the dynamic positioning errors reported in Section 4.3.1 were attributed to velocity saturation in the yaw/pitch control loop, but wind-induced UAV motion cannot be excluded as a contributing disturbance. Second, the link-budget model of Equation (1) neglects atmospheric effects, consistent with the short ranges tested, over which clear-air extinction at 1070 nm is expected to remain limited under standard visibility conditions; at the multi-hundred-meter-to-kilometer-scale ranges envisioned for operational use, atmospheric attenuation and turbulence-induced beam wander would need to be incorporated into the link budget. A systematic treatment of both effects, through synchronized wind measurement and a wavelength- and visibility-dependent extinction model, is left for future work.

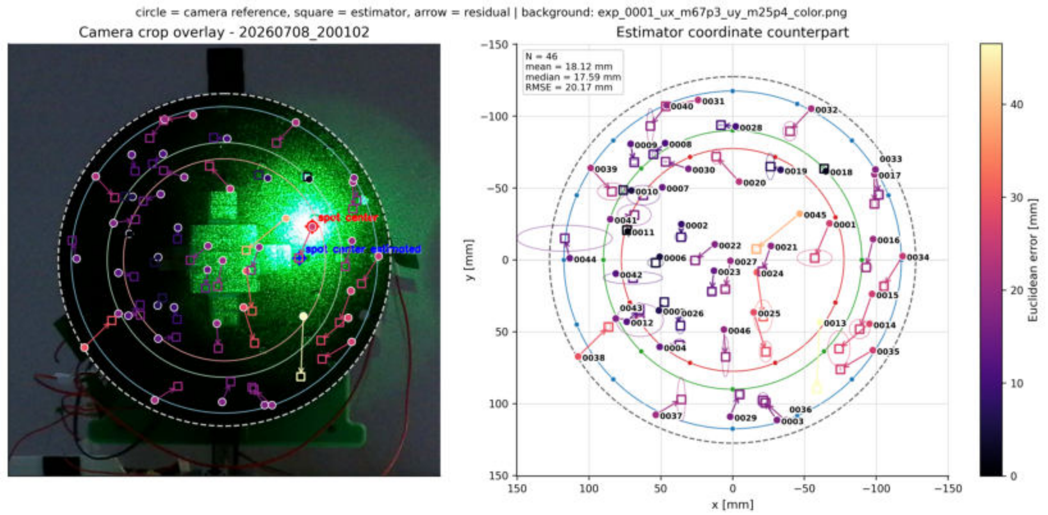


**Figure 13.** (**Left**) Overview map under stable evening light (N: = 46). (**Right**) Camera reference (circles) vs. photodiode-array estimate (squares), with residual vectors.

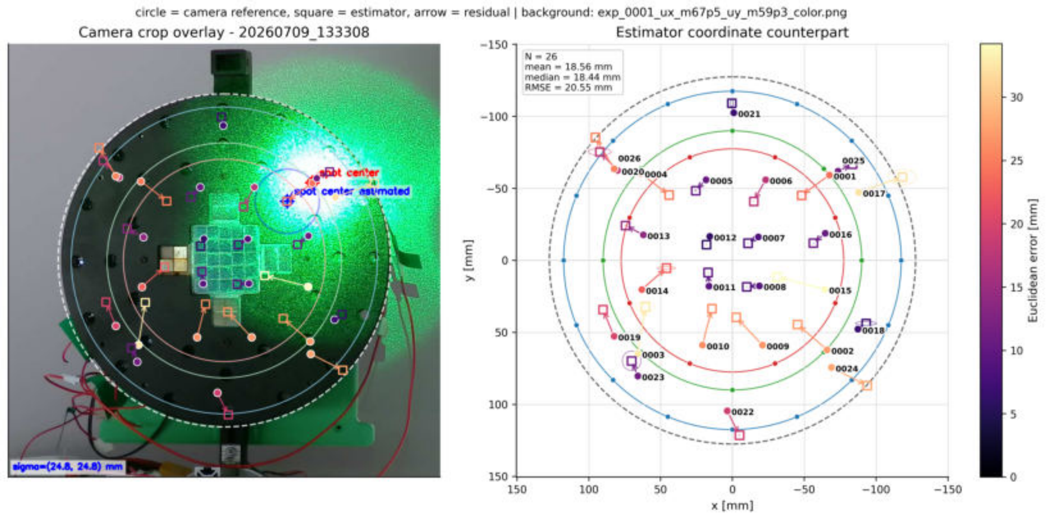


**Figure 14.** (**Left**) Overview map under variable daylight (N = 26). (**Right**) Camera reference (circles) vs. photodiode-array estimate (squares), with residual vectors.

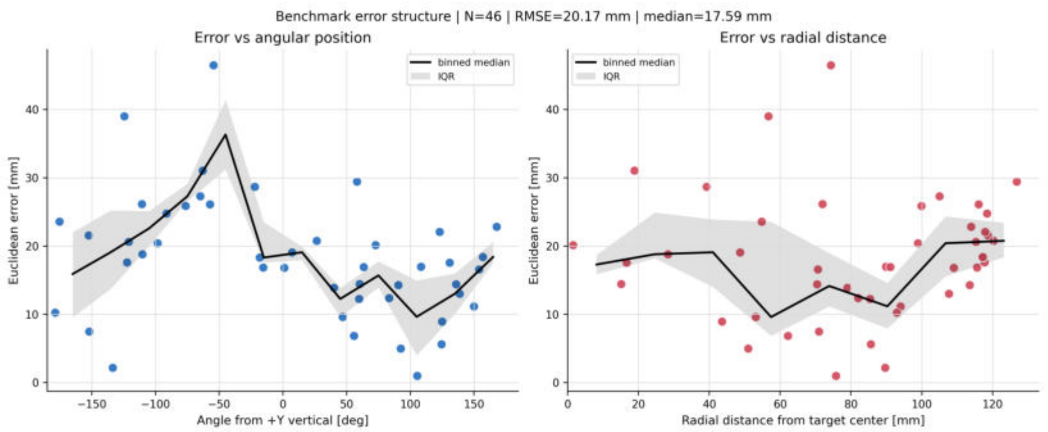


**Figure 15.** Euclidean localization error vs. (**Left**) angular position and (**Right**) radial distance from target center, stable evening light (N = 46).

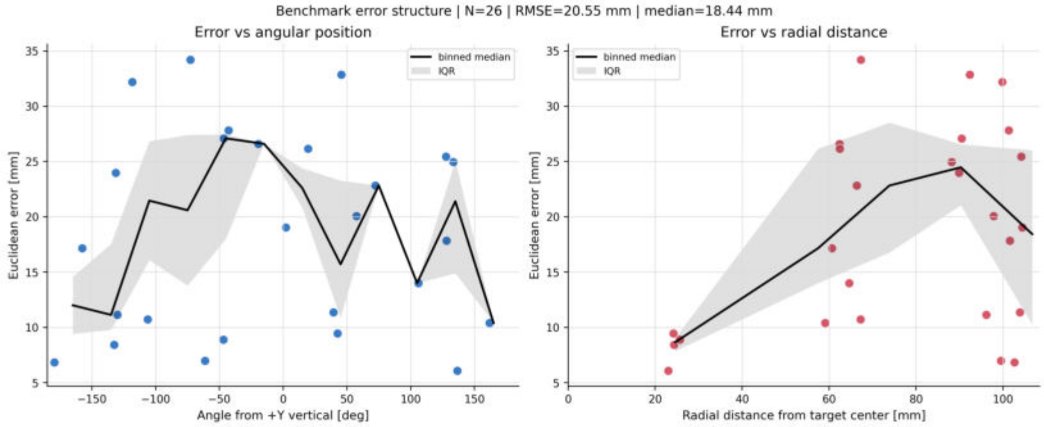


**Figure 16.** Euclidean localization error vs. (**Left**) angular position and (**Right**) radial distance from target center, variable daylight (N = 26).

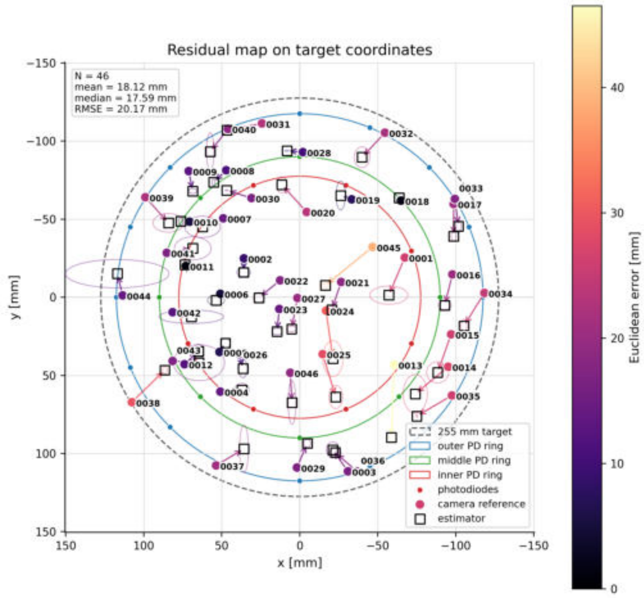


**Figure 17.** Residual map in target coordinates, stable evening light, N = 46.

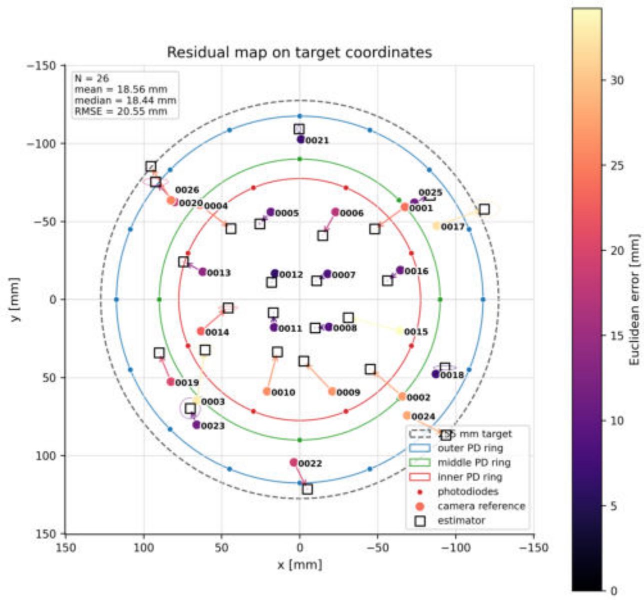


**Figure 18.** Residual map in target coordinates, variable daylight, N = 26.

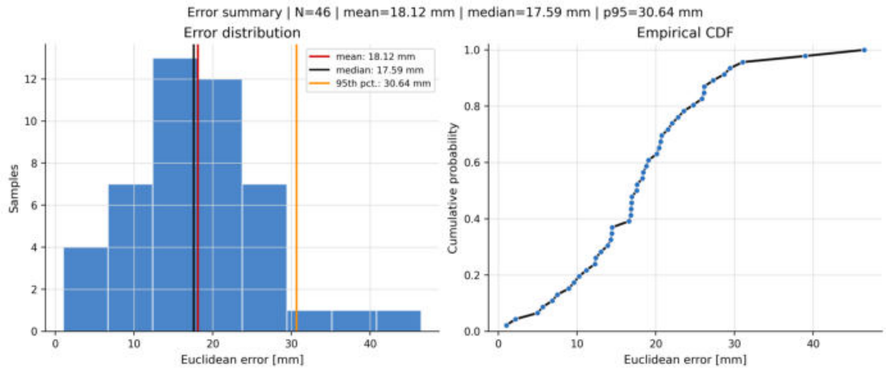


**Figure 19.** (**Left**) Error distribution (histogram) and (**Right**) empirical CDF, stable evening light (N = 46).

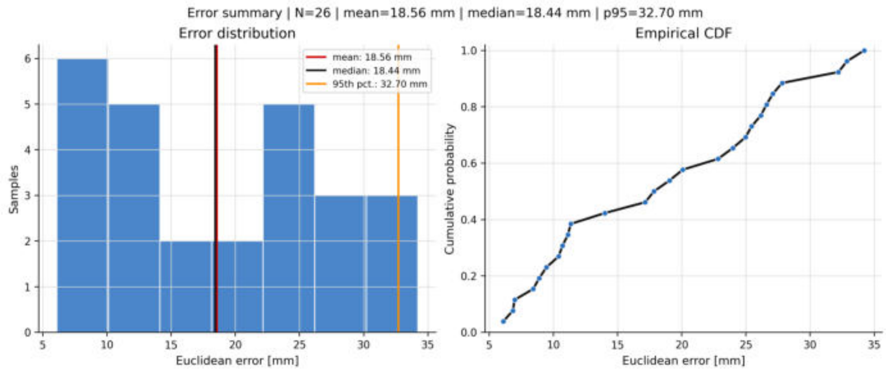


**Figure 20.** (**Left**) Error distribution (histogram) and (**Right**) empirical CDF, variable daylight (N = 26).

## 5. Conclusions

This paper presents a prototype system for wireless power transfer based on far-field laser to UAVs and reports an integrated experimental validation of its beam propagation, pointing, sensing, and telemetry subsystems. The beam propagation tests showed that, beyond approximately 40 m, the measured spot diameter follows the expected theoretical trend and can therefore support link-budget estimation. The experiments about the fine pointing demonstrated a near-linear relationship between commanded mirror steps and spot displacement, with limited cross-axis coupling, confirming the validity of the adopted steering model; the corresponding control law is intentionally a simple proportional mapping, and the reported step-response data provide only an initial, time-domain indication of closed-loop behavior, with a full control-theoretic characterization left for future work. The experimental campaign also highlighted the main limitation of the initial outdoor configuration: the misalignment between the East-North-Up (ENU) frame and the local ground reference frame. A structured calibration procedure based on the Kabsch algorithm, first verified in simulation and then applied to outdoor data, reduced this source of error and enabled static targeting performance consistent with the horizontal positioning uncertainty observed during the RTK validation tests. Tests on the receiver-side confirmed the reliability of the telemetry link, based on a low-latency ESP-NOW connection maintaining zero bit errors up to 170 m, and quantified for the first time the spot-localization accuracy of the photodiode array against an independent reference based on the camera (mean error $\approx$ 18 mm, RMSE $\approx$ 20 mm over a 255 mm target), with comparable performance under stable and variable ambient-light conditions and increasing error toward the outer edge of the receiver aperture. Overall, the results demonstrate that the proposed architecture is technically feasible and that its main subsystems operate consistently with the analytical models adopted in the design phase. Wind-disturbance rejection and atmospheric attenuation at long range, discussed qualitatively in Section 4.5, were not systematically characterized in the present campaign and remain open points for operational deployment. The work therefore provides an experimental basis for the development of persistent UAV laser-recharging systems. Future work will focus on closed-loop outdoor tracking, a full control-theoretic characterization of the fine-pointing loop, refined calibration of receiver-side sensing at operational stand-off distances, synchronized wind and atmospheric measurements, and extended end-to-end energy-transfer demonstrations under representative operational conditions.

**Author Contributions:** Conceptualization, D.E.S.; methodology, M.L. and D.E.S.; software, M.L.; validation, D.E.S., M.L. and F.Z.; formal analysis, M.L. and F.Z.; investigation, M.L.; data curation, F.Z.; writing—original draft preparation, D.E.S., M.L. and F.Z.; writing—review and editing, D.E.S.; visualization, M.L.; supervision, S.M.; project administration, S.M. All authors have read and agreed to the published version of the manuscript.

**Funding:** This research received no external funding.

**Data Availability Statement:** Dataset available on request from the authors.

**Conflicts of Interest:** Authors Marco Lecce and Federico Zambelli were employed by the company ORIS SRL. The remaining authors declare that the research was conducted in the absence of any commercial or financial relationships that could be construed as a potential conflict of interest.

## References

1. Mohamed, N.; Al-Jaroodi, J.; Jawhar, I.; Idries, A.; Mohammed, F. Unmanned Aerial Vehicles Applications in Future Smart Cities. *Technol. Forecast. Soc. Change* **2020**, *153*, 119293. [CrossRef]
2. Kiss, B.; Ballagi, A.; Kuczmann, M. Overview Study of the Applications of Unmanned Aerial Vehicles in the Transportation Sector. *Eng. Proc.* **2024**, *79*, 11 . [CrossRef]
3. Kumar, S.; Tiwari, A.; Ahirwar, Y.; Kumar, G.; Arafat, M.Y. The Rise of UAV-Based Smart Surveillance: A Systematic Review of Trends and Technologies. *IEEE Access* **2025**, *13*, 181553–181575. [CrossRef]
4. Zheng, Y.; Zhang, G.; Huan, Z.; Zhang, Y.; Yuan, G.; Li, Q.; Ding, G.; Lv, Z.; Ni, W.; Shao, Y.; et al. Wireless Laser Power Transmission: Recent Progress and Future Challenges. *Space Sol. Power Wirel. Transm.* **2024**, *1*, 17–26. [CrossRef]
5. Mohsan, S.A.H.; Qian, H.; Amjad, H. A Comprehensive Review of Optical Wireless Power Transfer Technology. *Front. Inf. Technol. Electron. Eng.* **2023**, *24*, 767–800. [CrossRef]
6. Ahmadi, K.; Serdijn, W.A. Advancements in Laser and LED-Based Optical Wireless Power Transfer for IoT Applications: A Comprehensive Review. *IEEE Internet Things J.* **2025**, *12*, 18887–18907. [CrossRef]
7. Lahmeri, M.A.; Kishk, M.A.; Alouini, M.S. Charging Techniques for UAV-Assisted Data Collection: Is Laser Power Beaming the Answer? *IEEE Commun. Mag.* **2022**, *60*, 50–56. [CrossRef]
8. Li, X.; Huang, G.; Wang, Z.; Zhao, B. Optics-Driven Drone. *Sci. China Inf. Sci.* **2024**, *67*, 124201. [CrossRef]
9. Nugent, T.; Bashford, D.J.; Bashford, T.; Sayles, T. 15 Years of Laser Power Beaming Demonstrations. In *Optical Power Delivery*; SPIE: Bellingham, WA, USA, 2025; Volume 13359 . [CrossRef]
10. Ochiai, N.; Toriumi, Y.; Kashiwakura, K.; Ota, S.; Yamaguchi, K.; Mando, Y.; Takeuchi, Y.; Takahashi, M.; Tsumura, Y. Demonstration of 15% Efficient Optical Wireless Power Transmission Over 1 km With Atmospheric Turbulence. *Electron. Lett.* **2025**, *61*, e70379. [CrossRef]
11. Nugent, T.J.; Kare, J.T. Laser Power Beaming for Defense and Security Applications. In *Unmanned Systems Technology XIII*; SPIE: Bellingham, WA, USA, 2011; Volume 8045, p. 804514. [CrossRef]
12. Chen, Q.; Zhang, D.; Zhu, D.; Shi, Q.; Gu, J.; Ai, Y. Design and Experiment for Realization of Laser Wireless Power Transmission for Small Unmanned Aerial Vehicles. In *AOPC 2015: Advances in Laser Technology and Applications*; SPIE: Bellingham, WA, USA, 2015; Volume 9671, pp. 133–139. [CrossRef]
13. Xu, W.; Wang, X.; Li, W.; Li, S.; Lu, C. Research on Test and Evaluation Method of Laser Wireless Power Transmission System. *EURASIP J. Adv. Signal Process.* **2022**, *2022*, 20. [CrossRef]
14. Sun, Y.; Shi, L.; Liu, K.; Sun, C.; Wu, Y.; Wan, R.; Guo, H. Research Progress on Laser Photovoltaic Converters for Laser Wireless Power Transmission. *Space Sol. Power Wirel. Transm.* **2026**, *3*, 19–36. [CrossRef]

15. Helmers, H. Photovoltaic Receivers for Optical Wireless Power Transfer and Communication. Fraunhofer Publica, 2025. In Proceedings of the 7th Optical Wireless and Fiber Power Transmission Conference (OWPT2025), Online/Venue Hybrid , Japan, 22–25 April 2025. [CrossRef]
16. Jiang, C.; Zhou, X.; Chen, H.; Liu, T. UAV Positioning Using GNSS: A Review of the Current Status. *Drones* **2026**, *10*, 91. [CrossRef]
17. Tavasci, L.; Nex, F.; Gandolfi, S. Reliability of Real-Time Kinematic (RTK) Positioning for Low-Cost Drones' Navigation across Global Navigation Satellite System (GNSS) Critical Environments. *Sensors* **2024**, *24*, 6096. [CrossRef] [PubMed]
18. Suzuki, T.; Inoue, D.; Amano, Y. Robust UAV Position and Attitude Estimation using Multiple GNSS Receivers for Laser-based 3D Mapping. In *2019 IEEE/RSJ International Conference on Intelligent Robots and Systems (IROS)*; IEEE: New York, NY, USA, 2019; pp. 4402–4408. [CrossRef]
19. Wang, X.; Su, X.; Liu, G.; Han, J.; Wang, R. Investigation of High-Precision Algorithm for the Spot Position Detection for Four-Quadrant Detector. *Optik* **2020**, *203*, 163941. [CrossRef]
20. Bao, R.; Yu, D.; Chen, F.; Lv, Z.; Xue, J.; Pan, Q.; Zhang, R. Research on High-Precision Position Detection Based on a Driven Laser Spot in an Extreme Ultraviolet Light Source. *Photonics* **2024**, *11*, 75. [CrossRef]
21. Chen, M.; Li, B.; Zhao, Y. Laser Source Fluctuation Compensation Method and High-Precision Location Algorithm for Laser Positioning Technology Based on Quadrant Photodetectors. In *International Conference on Optoelectronics and Optical Engineering*; SPIE: Bellingham, WA, USA, 2024; p. 132410P. [CrossRef]
22. de Celis, R.; Cadarso, L. Spot-Centroid Determination Algorithms in Semiactive Laser Photodiodes for Artillery Applications. *J. Sens.* **2019**, *2019*, 7938415. [CrossRef]
23. Siciliano, B.; Sciavicco, L.; Villani, L.; Oriolo, G. *Robotics: Modelling, Planning and Control*; Springer: Berlin/Heidelberg, Germany, 2010. [CrossRef]
24. Cadena, C.; Carlone, L.; Carrillo, H.; Latif, Y.; Scaramuzza, D.; Neira, J.; Reid, I.; Leonard, J.J. Past, Present, and Future of Simultaneous Localization and Mapping: Toward the Robust-Perception Age. *IEEE Trans. Robot.* **2016**, *32*, 1309–1332. [CrossRef]
25. Lyu, M.; Yang, J.; Qi, Z.; Xu, R.; Liu, J. Rigid Pairwise 3D Point Cloud Registration: A Survey. *Pattern Recognit.* **2024**, *151*, 110408. [CrossRef]
26. Kabsch, W. A Solution for the Best Rotation to Relate Two Sets of Vectors. *Acta Crystallogr. Sect. A* **1976**, *32*, 922–923. [CrossRef]
27. Schönemann, P.H. A Generalized Solution of the Orthogonal Procrustes Problem. *Psychometrika* **1966**, *31*, 1–10. [CrossRef]
28. Horn, B.K.P. Closed-Form Solution of Absolute Orientation Using Unit Quaternions. *J. Opt. Soc. Am. A* **1987**, *4*, 629–642. [CrossRef]
29. Umeyama, S. Least-Squares Estimation of Transformation Parameters Between Two Point Patterns. *IEEE Trans. Pattern Anal. Mach. Intell.* **1991**, *13*, 376–380. [CrossRef]
30. Arun, K.S.; Huang, T.S.; Blostein, S.D. Least-Squares Fitting of Two 3-D Point Sets. *IEEE Trans. Pattern Anal. Mach. Intell.* **1987**, *PAMI-9*, 698–700. [CrossRef] [PubMed]
31. Chaudhary, H.; Khatoon, S.; Singh, R.; Pandey, A. Fast Steering Mirror for Optical Fine Pointing Applications: A Review Paper. In *2018 3rd International Innovative Applications of Computational Intelligence on Power, Energy and Controls with Their Impact on Humanity (CIPECH)*; IEEE: New York, NY, USA, 2018; pp. 1–5. [CrossRef]
32. Sweeney, M.N.; Rynkowski, G.A.; Ketabchi, M.; Crowley, R. Design Considerations for Fast-Steering Mirrors (FSMs). In *Optical Scanning 2002*; SPIE: Bellingham, WA, USA, 2002; Volume 4773, pp. 63–73. [CrossRef]
33. Kim, J.G. System Integration Design of High-Performance Piezo-Actuated Fast-Steering Mirror for Laser Beam Steering System. *Sensors* **2024**, *24*, 6775. [CrossRef] [PubMed]
34. Pal, M.; Das, A.; Banerjee, K.; Dam, B. Modelling of Fast Steering Mirror Assembly: A Review of the Various Methodologies. *Optik* **2023**, *287*, 171108. [CrossRef]
35. Zhu, J.; Xu, Z.; Fu, D.; Hu, C. Laser Spot Center Detection and Comparison Test. *Photonic Sens.* **2018**, *8*, 302–310. [CrossRef]
36. Mi, X.; Sun, H.; Liu, Z.; Han, J. Research on Far-Field Spot Search and Centre Location Algorithms. *Front. Phys.* **2023**, *11*, 1230203. [CrossRef]
37. Zhao, H.; Wang, S.; Shen, W.; Jing, W.; Li, L.; Feng, X.; Zhang, W. Laser Spot Centering Algorithm of Double-Area Shrinking Iteration Based on Baseline Method. *Appl. Sci.* **2022**, *12*, 11302. [CrossRef]
38. Liang, M.; Wang, X. High-Precision Detection of Laser Spot Based on Gaussian Spot Model. In *Fourth International Conference on Optoelectronic Science and Materials*; SPIE: Bellingham, WA, USA, 2023; Volume 12748, pp. 1168–1172. [CrossRef]
39. Wang, X.; Xie, Y.; Liang, H.; Zhong, N. Analysis of Distortion Based on 2D MEMS Micromirror Scanning Projection System. *Micromachines* **2021**, *12*, 818. [CrossRef] [PubMed]